Ductile fracture prediction using enhanced CDM model with Lode angle-dependency for titanium alloy Ti-6Al-4V at room temperature

Kai Zhang, Houssem Badreddine, Khemais Saanouni

Version of Record: https://www.sciencedirect.com/science/article/pii/S0924013619304352
Manuscript_b5e3cd2afd92ffe88dc91ff1bbc9cc76

Ductile fracture prediction using enhanced CDM model with Lode angle-dependency for titanium alloy Ti-6Al-4V at room temperature

Kai Zhang [a,b], Houssem Badreddine [b], Khemais Saanouni [b]

[a] *Department of Engineering Mechanics, College of Pipeline and Civil Engineering, China University of Petroleum (East China), Qingdao, China*

[b] *ICD/LASMIS, University of Technology of Troyes, UMR 6281, CNRS, Troyes, France*

ABSTRACT:

Fully coupled ductile damage model considering strength-differential (SD) effect is proposed for simulation of metal forming processes for Ti-6Al-4V. The developed constitutive equations are based on non-associative plasticity theory under thermodynamically-consistent framework. The third stress invariant is added to Hill48 criterion to capture the SD effect. Lode angle-dependent enhanced fully coupled damage model is proposed to account for the loading path sensitivity on ductile damage initiation and growth. A detailed material parameters identification procedure is presented. The proposed model is implemented into the FE code Abaqus/Explicit through user defined subroutine VUMAT. The numerically predicted results obtained with the proposed model are compared to experimental data of Ti-6Al-4V and good agreement is observed.

Keywords: Anisotropy; Ductile damage; Lode angle; SD effect; Ti-6Al-4V alloy

1. Introduction

Titanium alloys are widely involved in aerospace applications such as aero engines, gas turbines and airframe components, due to their superior strength to weight ratio and heat resistance. They are also used in offshore petroleum industry, such as drilling risers, as a result of their excellent resistance to corrosion and high fatigue life. However, the high cost during manufacturing process is a major drawback of their large-scale industrial applications. Sheet metal forming is suitable for manufacturing titanium alloy components with a relatively low cost and high structure performance. The widely used Ti-6Al-4V alloy exhibits initial anisotropy and strength differential (SD) effect caused by the activation of twinning deformation mode, inducing complex problems in metal forming applications.

Finite element (FE) simulations provide efficient tools for predicting the forming capabilities, but the reliable numerical simulation results are highly dependent on the constitutive models. To accurately describe the plastic behavior of Ti-6Al-4V, the classical anisotropic plastic flow model developed by

Hill (1948) may not be appropriated. More sophisticated constitutive models which consider both plastic anisotropy and tension-compression asymmetry are required. Cazacu and Barlat (2004) proposed a yield function with both the second and third stress invariants, two linear transformations of stress tensor were applied to describe the yielding asymmetry in tension and compression, which referred as CB04. Later, Cazacu et al. (2006) developed another anisotropic and asymmetric yield function based on linear transformation tenor, referred as CPB06. The CB04 and CPB06 are widely applied for various Hexagonal Close-Packed (HCP) materials. Steglich et al. (2011) successfully predicted the earing during cup drawing test simulation for magnesium alloy ZM21 using CB04 criterion. Yoon et al. (2014) extended CB04 yield function for pressure sensitive metals. Khan et al. (2007) reported a low level of accuracy when applying CPB06 criterion for the prediction of the yield loci of Ti-6Al-4V. Additional linear transformations were added to this yield criterion by Plunkett et al. (2008) , named CPB06ex2 with two linear transformation tensors, while CPB06ex3 is based on three linear transformation tensors. A significant improvement of the accuracy in describing the anisotropy and SD effect for Ti-6Al-4V is reported by Gilles et al. (2011) when using the CPBex3 yield function compared to CPB06 and CPB06ex2. Unfortunately, this also means more material parameters are needed, in plane stress condition, about 25 material parameters for CPB06ex3, 17 material parameters for CPB06ex2, and 9 material parameters for CPB06. In this paper, a yield function extending the Hill48 criterion based on the third stress invariant ($J_3(\underline{\sigma})$) is applied. This yield function is similar to CB04 yield criterion, the difference is that our yield function can be easily recovered to Hill or Mises yield criteria through adjusting the values of simple material parameters.

When dealing with the case of strong anisotropy of both yield stress and plastic strain ratio, using the simple associative flow rule (AFR) with only one yield function may not work. It can be argued that the problem can be handled by using more complicated yield function with a large number of parameters, such as the Yld2004-18p criterion proposed by Barlat et al. (2005) or CPB06ex3 criterion developed by Plunkett et al. (2008). However, in the thermodynamically-consistent framework with definition of the state and dissipation potentials, the use of non-associative plasticity theory is suitable. During the last decades, the development and implementation of non-associative flow rule (non-AFR) in metal forming simulations were promising. Badreddine et al. (2010) developed the fully coupled damage model with non-AFR plasticity for damage prediction in metal forming. Taherizadeh et al.

(2015) observed that the accuracy of springback predictions was improved by using non-AFR with anisotropic hardening. Ghorbel et al. (2019) emphasized the importance of non-AFR on description of the DD13 material behavior and damage in bending process. In this paper, the constitutive model is developed with non-associative plasticity theory to achieve accurate description of the Ti-6Al-4V behavior.

The damage effect should be included in modeling the material behavior, they can be classified into three types: (1) uncoupled failure criteria; (2) weakly coupled models; (3) fully coupled models as those developed here in the framework of continuum damage mechanics (CDM).

The uncoupled approaches are based on specific failure criteria written in terms of stress or strain invariants giving the final fracture when their critical values are reached as stated in Johnson and Cook (1985). The advantage of these approaches are their simplicity by using the so-called failure indicators (criteria) which are easy to implement in FE software. However, these models do not consider the damage-induced softening effect on stress, stiffness and other material properties. Bai and Wierzbicki (2008) constructed a phenomenological model considering stress triaxiality and Lode angle effect to enhance fracture prediction capability. The uncoupled ductile fracture criterion proposed by Lou and Huh (2013) accurately describes the onset of ductile fracture in various stress states. However, the major weakness of these models lie in application to complex loading paths and large plastic strains.

In the weakly coupled damage models, i.e. GTN model proposed by Gurson (1977) and Tvergaard and Needleman (1984), the influence of ductile damage on the plastic flow is taken into account only throughout the yield function where the void volume fraction is introduced leading to a clear decrease of the equivalent stress when this voids volume fraction increases. The elastic stiffness (and other properties) is then not affected by damage (no decrease of the stiffness due to the damage occurrence). As reported by Cao (2013), a large number of material constants needs to be identified, some material constants have no physical meaning, which makes the calibration procedure of these models very difficult.

The CDM approach is based on the thermodynamics framework where the ductile damage is described by a scalar or tensorial variable (Lemaitre, 1985). Due to the strong coupling between the ductile damage and the material behavior, the overall material properties are deeply affected by the damage occurrence. This kind of approaches have been used for damage prediction in different kinds

of metal forming processes with various types of coupling assumptions as presented in the work of Saanouni (2006). Within the CDM approach, isotropic damage assumes that spherical micro-void cluster is homogeneously distributed without any privileged evolution direction at the local scale (i.e. at the material point seen as a representative volume element (RVE)). However, the anisotropic damage supposes that, at the RVE scale, the microcracks with different shapes and orientations are deeply influenced by material microstructure and its texture evolution related to the applied loading directions. In addition, The Lode angle effect is embedded in CDM approach by Cao et al. (2014) and Soyarslan et al. (2016),which allows predicting shear dominated fracture. Malcher and Mamiya (2014) suggested that the displacement at fracture occurrence is predicted more accurately by the CDM model with taking into account both stress triaxiality and Lode angle than the classical CDM model. Yue et al. (2019) investigated the Lode angle effect on damage evolution in various numerical simulations. These results confirmed that the fully coupled damage model with Lode angle dependency shows more accurate ductile fracture prediction under the wide range of loading paths. Even though the Lode angle effect is successfully included in CDM approach as shown in these works, the specific dependent form of the Lode angle in fully coupled damage model still need deeper exploration in order to improve the description of the isotropic ductile damage occurrence in metallic materials formed by large plastic deformation.

This paper aims to develop a fully coupled damage model to be applied for failure prediction during the forming of Ti-6Al-4V sheet metals. The constitutive equations are formulated within the framework of non-AFR theory with isotropic and kinematic hardening fully coupled with isotropic ductile damage. The SD effect is taken into account throughout the advanced anisotropic and asymmetric yield criterion. The CDM model is extended by a new Lode angle-dependent function to enhance the fracture prediction under different loading paths. Numerical aspects related to the local integration of the current constitutive equations are presented. Applications are made to the Ti-6Al-4V titanium alloy, the simulation results are discussed and compared to experimental data as well as other damage model simulation results.

2. Constitutive modeling

In this paper, the fully coupled damage model considering the strength differential effect is developed in the framework of the thermodynamics of irreversible processes with state variables. In finite strain theory, the decomposition the total transformation gradient into elastic $\underline{F}^e$ and plastic $\underline{F}^p$ part gives (Saanouni, 2012): $\underline{F} = \underline{F}^e \cdot \underline{F}^p$. For application to metal forming processes, the small elastic strain assumption is adopted based on the rotating frame formulation which leads to fulfil the objectivity requirement under finite plastic strains. By using the rotation tensor $\underline{Q}$, a rotated second-rank tensor $\underline{T}_Q$ can be obtained through $\underline{T}_Q = \underline{Q}^T \underline{T}\, \underline{Q}$. In this work, the evolution of $\underline{Q}$ is defined in kinematical way based on Green-Naghdi rotation frame (Badreddine et al., 2010).

The following state variables are used in the current formulation: $(\underline{\varepsilon}^e, \underline{\sigma})$ for small elastic strain and Cauchy stress tensor; $(\underline{\alpha}, \underline{X})$ for kinematic hardening; (r, R) for isotropic hardening; and (d, Y) for isotropic ductile damage.

In order to introduce the strong coupling between the effect of ductile damage and the other mechanical fields, the framework of the total energy equivalence assumption (Saanouni, 2012) is performed in such a manner that the couples of effective state variables $(\underline{\tilde{\varepsilon}}^e, \underline{\tilde{\sigma}})$, $(\underline{\tilde{\alpha}}, \underline{\tilde{X}})$ and $(\tilde{r}, \tilde{R})$ are defined in a fictitious undamaged, but locally rotated, configuration by:

$$\underline{\tilde{\varepsilon}}^e = \sqrt{1-d}\,\underline{\varepsilon}^e \quad \text{and} \quad \underline{\tilde{\sigma}} = \frac{\underline{\sigma}}{\sqrt{1-d}} \tag{1}$$

$$\underline{\tilde{\alpha}} = \sqrt{1-d}\,\underline{\alpha} \quad \text{and} \quad \underline{\tilde{X}} = \frac{\underline{X}}{\sqrt{1-d}} \tag{2}$$

$$\tilde{r} = \sqrt{1-d^{\gamma}}\, r \quad \text{and} \quad \tilde{R} = \frac{R}{\sqrt{1-d^{\gamma}}} \tag{3}$$

The stress-like variables obtained from appropriate state potentials which are expressed by the effective state variables (Eq. (1)-(3)), are shown in Table 1, where ρ denotes the material density, $\underline{\underline{\Lambda}} = 2\mu_e \underline{\underline{1}} + \lambda_e \underline{1} \otimes \underline{1}$ denotes the isotropic elastic fourth-rank operator expressed by the Lame's constants μ_e and λ_e, C and Q are kinematic and isotropic hardening modules.

Table 1 Stress-like variables and evolution equations

	Stress-like variables	Evolution equations
Cauchy stress	$\underline{\sigma} = \rho\dfrac{\partial \Psi}{\partial \underline{\varepsilon}^e} = (1-d)\underline{\underline{\Lambda}} : \underline{\varepsilon}^e$	$\underline{D}^p = \dot{\lambda}\dfrac{\partial F}{\partial \underline{\sigma}} = \dot{\lambda}\underline{n} = \dfrac{\dot{\lambda}}{\sqrt{1-d}}\tilde{\underline{n}}$ with $\tilde{\underline{n}} = \dfrac{\|\underline{Z}\|_H \left(\underline{\underline{H}} : \underline{Z}\right) - \dfrac{w}{3}\|\underline{Z}\|_{J3}\,\underline{Z}'^{-T} : \underline{\underline{H}}'}{\left[\|\underline{Z}\|_H^3 - w\|\underline{Z}\|_{J3}\right]^{2/3}}$
Kinematic hardening	$\underline{X} = \rho\dfrac{\partial \Psi}{\partial \underline{\alpha}} = \dfrac{2}{3}(1-d)C\underline{\alpha}$	$\dot{\underline{\alpha}} = -\dot{\lambda}\dfrac{\partial F}{\partial \underline{X}} = \dot{\lambda}(\dfrac{1}{\sqrt{1-d}}\tilde{\underline{n}} - a\underline{\alpha})$
Isotropic hardening	$R = \rho\dfrac{\partial \Psi}{\partial r} = (1-d^{\gamma})Qr$	$\dot{r} = -\dot{\lambda}\dfrac{\partial F}{\partial R} = \dot{\lambda}\left(\dfrac{1}{\sqrt{1-d^{\gamma}}} - br\right)$
Damage governing force	$Y = -\rho\dfrac{\partial \Psi}{\partial d} = Y^e + Y^{\alpha} + Y^r$ $= \dfrac{1}{2}\underline{\varepsilon}^e : \underline{\underline{\Lambda}} : \underline{\varepsilon}^e + \dfrac{1}{3}C\underline{\alpha} : \underline{\alpha} + \dfrac{1}{2}\gamma d^{\gamma-1}Qr^2$	$\dot{d} = \dot{\lambda}\dfrac{\partial F}{\partial Y} = \dfrac{\dot{\lambda}}{(1-d)^{\beta}}\left(\dfrac{\langle Y - Y_0\rangle}{S\left(\bar{\theta}_L\right)}\right)^s$

The evolution equations, given in Table 1, are obtained from the dissipation potential using the well-known generalized normality rule (Saanouni, 2012). The total dissipation potential $F(\underline{\sigma},\underline{X},R,Y,d)$, a convex function of the stress-like variables, is the sum of a plastic dissipation potential $F_p(\underline{\sigma},\underline{X},R,d)$ and a damage dissipation potential $F_d(d,Y)$:

$$F(\underline{\sigma},\underline{X},R,Y,d) = \underbrace{\frac{\Sigma_{eq}^p}{\sqrt{1-d}} - \frac{R}{\sqrt{1-d^{\gamma}}} + \frac{3a(\underline{X}:\underline{X})}{4C(1-d)} + \frac{bR^2}{2Q(1-d^{\gamma})}}_{F_p(\underline{\sigma},\underline{X},R,d)} + \underbrace{\frac{S\left(\bar{\theta}_L\right)}{(s+1)(1-d)^{\beta}}\left\langle\frac{Y-Y_0}{S\left(\bar{\theta}_L\right)}\right\rangle^{(s+1)}}_{F_d(d,Y)} \tag{4}$$

where the material parameters a and b define the nonlinear evolution of kinematic and isotropic hardening respectively; while S, s, Y_0, β, γ are damage parameters (Lemaitre and Chaboche, 1994).

The quadratic anisotropic Hill48 equivalent stress is modified by including the third stress invariant (Zhang et al., 2018) to describe the tension-compression asymmetry of yielding(or SD effect) exhibited by the HCP material:

$$\Sigma_{eq}^i = \left(\left\|\underline{Z}^i\right\|_H^3 - w\left\|\underline{Z}^i\right\|_{J3}\right)^{1/3} \quad with \quad \begin{cases}\left\|\underline{Z}^i\right\|_H = \sqrt{(\underline{S}-\underline{X}) : \underline{\underline{H}}_i : (\underline{S}-\underline{X})} \\ \left\|\underline{Z}^i\right\|_{J3} = \det\left(\underline{Z}'^i\right) = \det\left(\underline{\underline{H}}_i' : (\underline{S}-\underline{X})\right)\end{cases} \quad (i = \{c, p\}) \tag{5}$$

where w is a kind a material parameter controlling the contribution of the third invariant of the Cauchy stress tensor. The equivalent stresses used in both the yield criterion $f_c(\underline{\sigma},\underline{X},R,d)$ and in the dissipation potential $F_p(\underline{\sigma},\underline{X},R,d)$ are characterized by two fourth-rank symmetric tensors $\underline{\underline{H}}$ and $\underline{\underline{H}}'$

as shown in Eq. (7), each of them is represented by six anisotropy parameters. In the framework of non-associative theory, the equivalent stress Σ_{eq}^{c} in yield criterion (Eq.(6)) and the counterpart Σ_{eq}^{p} in the dissipation potential (Eq. (4)) are different from each other since different values of the anisotropic parameters are used to control the initial anisotropy and asymmetry ($\underline{\underline{H}}_c \neq \underline{\underline{H}}_p$ and $\underline{\underline{H}}'_c \neq \underline{\underline{H}}'_p$),

$$f_c(\underline{\sigma}, \underline{X}, R, d) = \frac{\Sigma_{eq}^{c}}{\sqrt{1-d}} - \frac{R}{\sqrt{1-d^{\gamma}}} - \sigma_y \leq 0 \tag{6}$$

where σ_y denotes the yield stress. The material parameter w in Eq. (5) is set to $w = 1.0$ when SD effect is taken into account, while if $w = 0.0$ the Hil48 quadratic equivalent stress is obtained, while in between 0.0 and 1.0 the contribution of the third stress invariant is minimized or maximized. Finally, the von Mises equivalent stress can be recovered when $\underline{\underline{H}} = \frac{3}{2}\underline{\underline{I}}^{dev} = \frac{3}{2}(\underline{\underline{I}} - \frac{1}{3}\underline{1} \otimes \underline{1})$.

$$\underline{\underline{H}}_i = \begin{bmatrix} G_i + H_i & -H_i & -G_i & 0 & 0 & 0 \\ -H_i & H_i + F_i & -F_i & 0 & 0 & 0 \\ -G_i & -F_i & F^i + H_i & 0 & 0 & 0 \\ 0 & 0 & 0 & 2N_i & 0 & 0 \\ 0 & 0 & 0 & 0 & 2M_i & 0 \\ 0 & 0 & 0 & 0 & 0 & 2L_i \end{bmatrix} \text{ and } \underline{\underline{H}}'_i = \begin{bmatrix} G'_i + H'_i & -H'_i & -G'_i & 0 & 0 & 0 \\ -H'_i & H'_i + F'_i & -F'_i & 0 & 0 & 0 \\ -G'_i & -F'_i & F' + H'_i & 0 & 0 & 0 \\ 0 & 0 & 0 & 2N'_i & 0 & 0 \\ 0 & 0 & 0 & 0 & 2M'_i & 0 \\ 0 & 0 & 0 & 0 & 0 & 2L'_i \end{bmatrix} \tag{7}$$

It has been proved that the ductility of some materials is dependent on the stress state which is defined by the stress invariants, especially the Lode angle (Xue and Wierzbicki, 2008) defined as the ratio between the third over the second stress invariants. Different damage and fracture models have included the Lode angle effect (Bai and Wierzbicki, 2008; Cao et al., 2014), which makes enhancements in shear dominant fracture prediction in metal forming. Since the parameter s in our damage evolution equation controls the material ductility, it is expressed by a new Lode angle-dependent function according to:

$$S(\bar{\theta}_L) = S_{sh} + (S_{ten} - S_{sh})\,\mathrm{Tanh}(\left|\bar{\theta}_L\right|^{\xi_s}) \tag{8}$$

where the parameter S_{sh} , S_{ten} and ξ_s are used to adjust the value of s according to different stress states. The normalized Lode angle $\bar{\theta}_L\,(-1 \leq \bar{\theta}_L \leq 1)$ is then given by:

$$\bar{\theta}_L = 1 - \frac{6\theta_L}{\pi} = 1 - \frac{2}{\pi}\arccos\left(\frac{3\sqrt{3}J_3}{2J_2^{3/2}}\right) \tag{9}$$

It should be noted that the rotated deviator of stress tensor $\underline{S}_Q$ obtained from rotation frame does not affect the normalized Lode angle as shown below:

$$\det(\underline{S}_Q) = \det(\underline{Q}^T \underline{S} \underline{Q}) = \det(\underline{Q}^T) \cdot \det(\underline{S}) \cdot \det(\underline{Q}) = \det(\underline{Q}^T \underline{Q}) \cdot \det(\underline{S}) = \det(\underline{S}) \tag{10}$$

Fig. 1a illustrates the effect of the parameter ξ_s on the evolution of ductility parameter S when considering S_{ten}=2.0 and S_{sh}=1.0, the value of S is symmetric with respect to the vertical axis defined by $\bar{\theta}_L$=0.0, the smallest value of S is obtained for $\bar{\theta}_L$=0.0, then it increases symmetrically at both the negative and positive sides of $\bar{\theta}_L$. The parameter ξ_s controls how the value of S evolves according with $\bar{\theta}_L$, when ξ_s increases, the curve becomes more flat at the middle part (corresponding to the small absolute values of $\bar{\theta}_L$). As shown in Fig. 1b, the evolution curve is convex when $S_{ten} > S_{sh}$, otherwise, it is concave when $S_{ten} < S_{sh}$, and the maximum and minimum values of S can be achieved by varying the values of S_{ten} and S_{sh}.

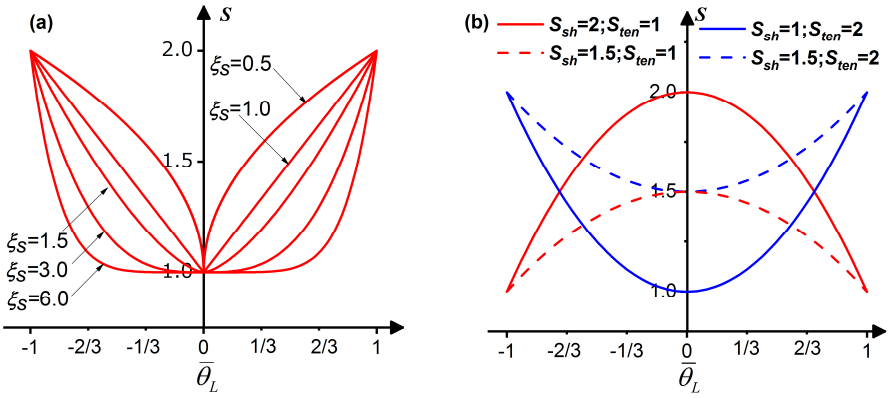

Fig. 1. Influence of normalized Lode angle $\bar{\theta}_L$ on the ductility parameter S : (a) for different values of ξ_s considering S_{ten}=2.0 and S_{sh}=1.0; (b) for different values of S_{ten} and S_{sh} considering ξ_s=2.0.

The iso-damage surfaces (or fracture loci) including the Lode angle effect are plotted in Fig. 2. The circular surface is obtained when $S_{ten} = S_{sh}$ (no Lode angle effect). When $S_{ten} < S_{sh}$, the shape of iso-damage surface at constant stress triaxiality varies from a right hexagon to a six-point star. When $S_{ten} > S_{sh}$, the iso-damage surface at constant stress triaxiality is transferred to a shape of flower with six petals. Note that for this case of isotropic plasticity, the iso-damage surfaces have a $\pi/3$ symmetry so that fracture locus at six vertices with $\bar{\theta}_L = \pm 1$ are the same. It should be bear in mind that the ductile fracture tends to occur at the region between the two vertices (shear or plane strain mode), which has proved by experiments reported in the work of Lou and Huh (2013).

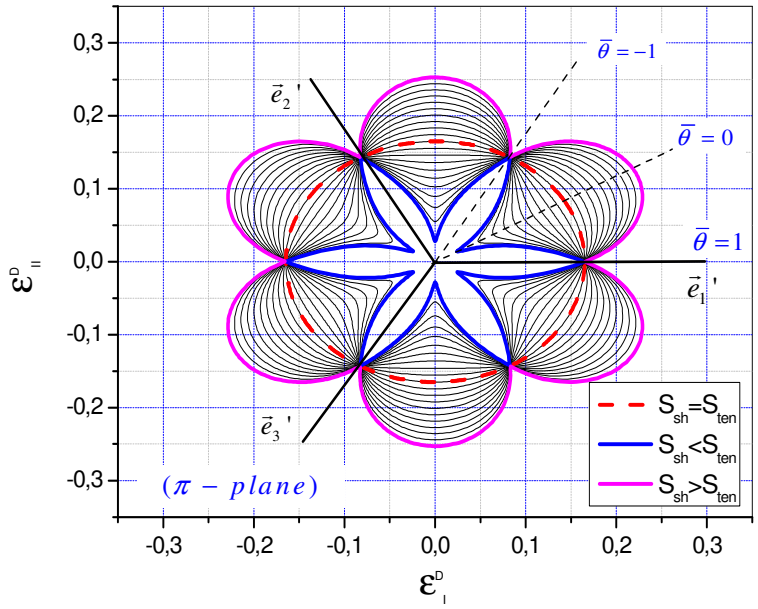

Fig. 2. Effect of (S_{ten}-S_{sh}) on the iso-damage surface plotted in the deviatoric strain plane.

3. Numerical aspects

The above presented constitutive equations are implemented into ABAQUS/Explicit FE code via the user subroutine VUMAT. The numerical integration algorithm is based on the fully implicit backward Euler scheme combined with the asymptotic scheme (Saanouni, 2012), which leads to the following discretized equations:

$$\underline{\sigma}_{n+1}(\Delta\lambda, \underline{n}_{n+1}, d_{n+1}) = \frac{1-d_{n+1}}{1-d_n}\underline{\sigma}^{tr}_{n+1} - 2(1-d_{n+1})\mu_e \Delta\lambda \underline{n}_{n+1} \tag{11}$$

$$\underline{X}_{n+1}(\Delta\lambda, \underline{n}_{n+1}, d_{n+1}) = \frac{2}{3}(1-d_{n+1})C\left[\underline{\alpha}_n e^{-a\Delta\lambda} + \frac{(1-e^{-a\Delta\lambda})}{a\sqrt{1-d_{n+1}}}\underline{n}_{n+1}\right] \tag{12}$$

$$R_{n+1}(\Delta\lambda, d_{n+1}) = (1-d_{n+1})Q\left[r_n e^{-b\Delta\lambda} + \frac{1-e^{-b\Delta\lambda}}{b\sqrt{1-d_{n+1}}}\right] \tag{13}$$

$$Y_{n+1}(\Delta\lambda, \underline{n}_{n+1}, d_{n+1}) = \frac{1}{2}\underline{\varepsilon}^e_{n+1} : \underline{\underline{\Lambda}} : \underline{\varepsilon}^e_{n+1} + \frac{1}{3}C\underline{\alpha}_{n+1} : \underline{\alpha}_{n+1} + \frac{1}{2}Qr^2_{n+1} \tag{14}$$

$$d_{n+1}(\Delta\lambda, \underline{n}_{n+1}, d_{n+1}) = d_n + \frac{\Delta\lambda}{(1-d_{n+1})^\beta}\left\langle \frac{Y_{n+1}(\Delta\lambda, \underline{n}_{n+1}, d_{n+1}) - Y_0}{S(\bar{\theta}_L)} \right\rangle^s \tag{15}$$

These variables written at time $t_{n+1} = t_n + \Delta t$ are obtained by assuming all the state variables are known at time t_n. Furthermore, they should be admissible with the yield criterion given at time t_{n+1}:

$$f_{n+1}(\underline{\sigma}_{n+1}, \underline{X}_{n+1}, R_{n+1}, d_{n+1}) = \frac{\Sigma^c_{eq(n+1)}}{\sqrt{1-d_{n+1}}} - \frac{R_{n+1}}{\sqrt{1-d^\gamma_{n+1}}} - \sigma_y = 0 \tag{16}$$

This system (from Eq.(11) to Eq.(16)) is reduced to three equations with three unknowns(d_{n+1},$\underline{\tilde{n}}_{n+1}$ and $\Delta\lambda$), as shown in Eq.(17), then linearized and solved using the Newton-Raphson(N-R) method. The detailed local integration scheme is given in Table 2.

$$\begin{cases} f_{n+1}(\Delta\lambda, d_{n+1}, \underline{\tilde{n}}_{n+1}) = \dfrac{\Sigma^{c}_{eq(n+1)}}{\sqrt{1-d_{n+1}}} - \dfrac{R_{n+1}}{\sqrt{1-d^{\gamma}_{n+1}}} - \sigma_{y} = 0 \\ g_{n+1}(\Delta\lambda, d_{n+1}, \underline{\tilde{n}}_{n+1}) = d_{n+1} - d_{n} - \dfrac{\Delta\lambda}{(1-d_{n+1})^{\beta}} \left\langle \dfrac{Y_{n+1}(\Delta\lambda, \underline{\tilde{n}}_{n+1}, d_{n+1}) - Y_{0}}{S(\bar{\theta}_{L})} \right\rangle^{s} = 0 \\ \underline{h}_{n+1}(\Delta\lambda, d_{n+1}, \underline{\tilde{n}}_{n+1}) = \underline{\tilde{n}}_{n+1} - \dfrac{\left(3\left\|\underline{Z}^{p}\right\|_{H}\left(\underline{\underline{H}} : \underline{Z}\right) - w\left\|\underline{Z}\right\|_{J3}\underline{Z}'^{-T} : \underline{\underline{H}}'\right)_{n+1}}{3(\Sigma^{p}_{eq})^{2}_{(n+1)}} = 0 \end{cases} \tag{17}$$

Table 2 Local integration algorithm

- Initialize all the kinematic and state variables, then recover them at time t_n
- Use the rotation tensor $\underline{Q}$ to rotate the tensors $\left(\underline{\sigma}_n, \underline{X}_n, \underline{\alpha}_n\right)$
- Elastic predictor: compute trial stress

  $\{\Delta\lambda = 0\} \Rightarrow \left\{\Delta\underline{\varepsilon}^{p} = \underline{0},\ \Delta\underline{\alpha} = \underline{0},\ \Delta r = 0,\ \Delta d = 0\right\}$

  $\Rightarrow \left\{\underline{\varepsilon}^{p}_{n+1} = \underline{\varepsilon}^{p}_{n}, \underline{\alpha}_{n+1} = \underline{\alpha}_{n}, r_{n+1} = r_{n}, d_{n+1} = d_{n}\right\}$

  Trial stress: $\underline{\sigma}^{tr}_{n+1} = \underline{\sigma}_{n} + (1-d_{n})\underline{\underline{\Lambda}} : \Delta\underline{\varepsilon}$
- Check for yielding:

  IF $f^{tr}_{n+1}(\underline{\sigma}^{tr}_{n+1}, \underline{X}_{n}, R_{n}, d_{n}) \le 0$ **THEN**

  $$\begin{cases} \underline{\sigma}_{n+1} = \underline{\sigma}^{tr}_{n+1}, & \underline{\varepsilon}^{p}_{n+1} = \underline{\varepsilon}^{p}_{n} \\ \underline{X}_{n+1} = \underline{X}_{n}, & \underline{\alpha}_{n+1} = \underline{\alpha}_{n} \\ R_{n+1} = R_{n}, & r_{n+1} = r_{n} \\ Y_{n+1} = Y_{n}, & d_{n+1} = d_{n} \end{cases}$$

  ELSE CONTINUE
- Plastic correction:
  - Solve the system in Eq.(17) using the N-R method
  - Update the variables in Eq.(11)-Eq.(15)
  - Update the kinematical variables

  END IF

4. Application to titanium alloy Ti-6Al-4V

4.1 Parameters identification

The calibration of the material parameters is conducted through two steps (Zhang et al., 2019). First, the material parameters related to elastoplastic behavior with hardening but without damage are calibrated. Within this step, the elasticity parameters are obtained from uniaxial tension test. The anisotropy parameters are determined using both yield stresses and *R*-values for different material

orientations with respect to the rolling direction. The hardening parameters are identified using the initial stage of the plastic flow with assumption that damage effect is negligible at this initial stage. Second, the damage variables are determined through the notched tension and shear tests (Yue et al., 2015; Zhuang et al., 2017). This whole pro

The anisotropy parameters, given in Table 3, are determined by minimizing the objective function in the following form:

$$Min(\Delta) = Min\left[\omega_\sigma \sum_{i=T}^{C}\sum_{\theta=0}^{90}\left(\frac{\sigma_\theta^{i\_\exp}}{\sigma_\theta^{i\_\mathrm{sim}}}-1\right)^2 + \omega_r \sum_{i=T}^{C}\sum_{\theta=0}^{90}\left(\frac{r_\theta^{i\_\exp}}{r_\theta^{i\_\mathrm{sim}}}-1\right)^2 + \omega_{\sigma b}\sum_{i=T}^{C}\left(\frac{\sigma_b^{\mathrm{i}\_\exp}}{\sigma_b^{i\_\mathrm{sim}}}-1\right)^2 + \omega_{rb}\sum_{i=T}^{C}\left(\frac{r_b^{\mathrm{i}\_\exp}}{r_b^{\mathrm{i}\_\mathrm{sim}}}-1\right)^2\right] \tag{18}$$

where σ_θ^i and r_θ^i are yield stresses and Lankford coefficients (R-value) with orientations θ from the rolling direction($\theta = 0^\circ$), σ_b^i and r_b^i are the equi-biaxial values. The index i denotes the tension (i=T) and compression (i=C) loading paths. The superscript 'exp' and 'sim' means the data from experiments and simulations. The weighting parameters switch the cases between non-AFR ($\{\omega_\sigma = \omega_{\sigma b} = \omega_r = \omega_{rb} = 1\}$) and AFR theory ($\{\omega_\sigma = \omega_{\sigma b} = 1, \omega_r = \omega_{rb} = 0\}$ or $\{\omega_\sigma = \omega_{\sigma b} = 0, \omega_r = \omega_{rb} = 1\}$). The analytical expressions of yield stresses and R-values are given in Appendix A.

Table 3 Calibrated anisotropy parameters of Ti-6Al-4V using experiential data in (Gilles et al., 2011)

F_c	G_c	H_c	N_c	F_c'	G_c'	H_c'	N_c'
0.51268	0.57484	0.37089	1.53660	-0.42908	-0.19191	0.72270	0.63820
F_p	G_p	H_p	N_p	F_p'	G_p'	H_p'	N_p'
1.21938	1.61436	1.48815	3.03887	-0.61843	1.38874	1.21394	-1.27768

Fig. 3 shows the numerically predicted yield surfaces compared to experimentally measured points. The experimental results were all obtained by conducting quasi-static tensile and compressive tests using standard tensile specimens which were cut from the sheet by milling as reported in (Gilles et al., 2011). It is worth noting that the compression tests were treated using special designed comb-shaped dies apparatus developed by Kuwabara et al. (2009) to perform the compression tests on thin sheet specimens. For comparison purpose, the predicted surface using Hill yield function is also presented (using identified parameters in Table A.1 of Appendix A), it shows that the Hill yield function can only describe the initial anisotropy in tension. However, the proposed model could capture accurately the anisotropy and SD effect of Ti-6Al-4V titanium alloy.

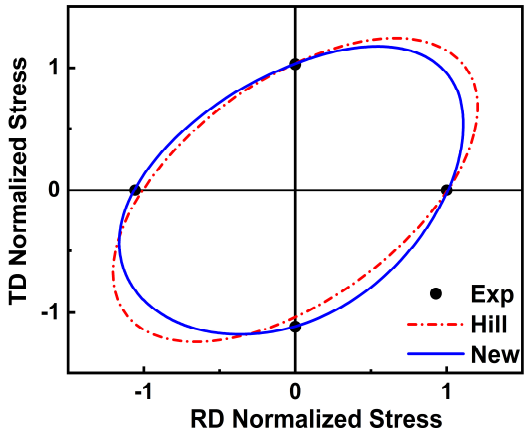

Fig. 3. Comparisons of numerically predicted yield surfaces with experimental data

The tensile and compressive yield stresses at different material orientations with respect to the rolling direction calculated from Hill and new proposed model are compared with experimental data in Fig. 4. 'Hill_R' and 'Hill_S' represent the predicted results using parameters calibrated with AFR strain-ratio and stress-ratio based experimental data respectively. The difference of predicted tensile stresses by the current model and Hill criterion with stress-ratio is slight in tension, both can fit most of the experimental points. The predicted compressive yield stresses according to Hill criterion induce a significant deviation with experimental results, while the current yield function shows quite good agreement with experimental data in both tension and compression tests. Fig. 5 shows the *R*-values as described by Hill and current yield function under both AFR and non-AFR conditions. It is noticed that only the new proposed model under non-AFR theory shows the best fitting with experimental *R*-values. Therefore, the proposed model with non-AFR captures well the anisotropies in *R*-values and yield stresses.

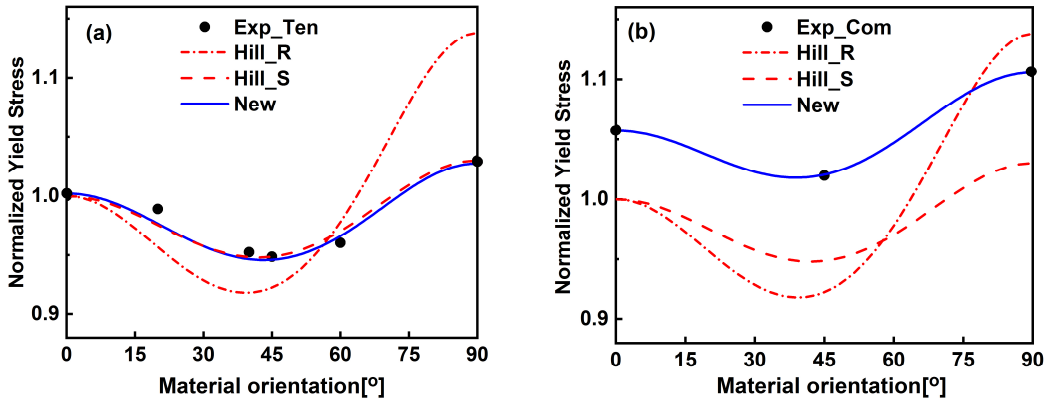

Fig. 4. Comparisons of predicted yield stresses according to Hill and new proposed model with experimental data: (a) yield stresses in tension; (b) yield stresses in compression.

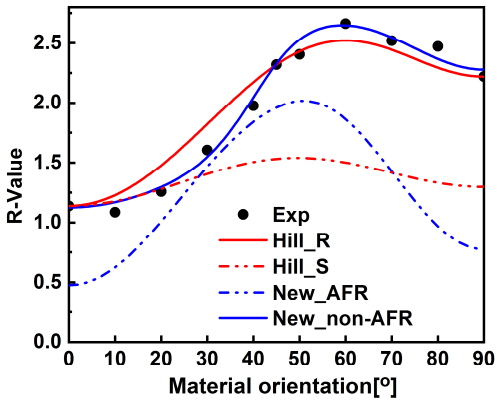

Fig. 5. Comparisons of predicted R-values with experimental data

Since the inherent damage-plasticity full coupling character of CDM formulation, the identification for the hardening and damage parameters may seem to be puzzled. In this paper, an uncoupled version of the proposed model is used to determine the hardening parameters by assuming that damage effect is negligible at the early stage of plasticity. Fig. 6 shows the predicted force-displacement curve using uncoupled model with calibrated material parameter in Table 4. The simulation result shows good accordance with experimental results (Allahverdizadeh et al., 2015) before the displacement 1.0mm when no significant damage induced softening or necking is observed.

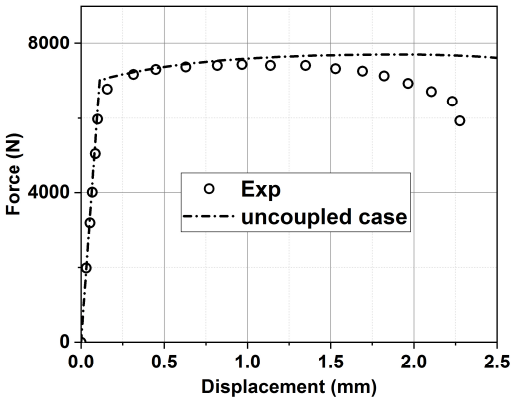

Fig. 6. Numerical simulated force-displacement curve compared to experimental data for uniaxial round bar tensile test.

Once the parameters related to anisotropy and hardening are determined, tensile tests of shear specimen and notched specimens with different radius (R=6.67mm, 10.0mm and 20.0mm) (Allahverdizadeh et al., 2015) are used to determine the damage related material parameters . The design and FEM mesh for the specimens are illustrated in Fig. 7. In the central area of the specimen, where the fracture is expected to occur, the mesh size about 0.1mm is used on the plate surface and through thickness direction. This minimum mesh size will be used inside the localization zones for all

the simulations in order to avoid the well-known mesh dependence related to the local models with damage-induced softening (see (Saanouni and Hamed, 2013) for generalized nonlocal micromorphic models). A noteworthy fact is that the current enhanced CDM model has the capability to predict the shear-dominant fracture since its Lode angle dependency. However, to determine the parameters S_{sh} and S_{ten}, several tests are needed such as simple shear test (i.e. $\bar{\theta}_L = 0$) and tensile tests with notched specimen. Efforts have been made by Yin et al. (2015) and Traphöner et al. (2018) to pursuit the simple shear tests, in this paper we limit ourselves to use the systematic experiments carried out at Politecnico di Milano (Allahverdizadeh, 2014; Allahverdizadeh et al., 2015; Giglio et al., 2012) for Ti-6Al-4V to determine the material parameters. The influence of the damage parameters (s, β, γ, Y_0) on the damage evolution has been elaborated in (Saanouni, 2012). The critical damage value is $d_c = 0.99$ and constant values are fixed to two parameters (γ=4.0 and Y_0=0.0). The calibrated hardening and damage parameters of Ti-6Al-4V are shown in Table 4.

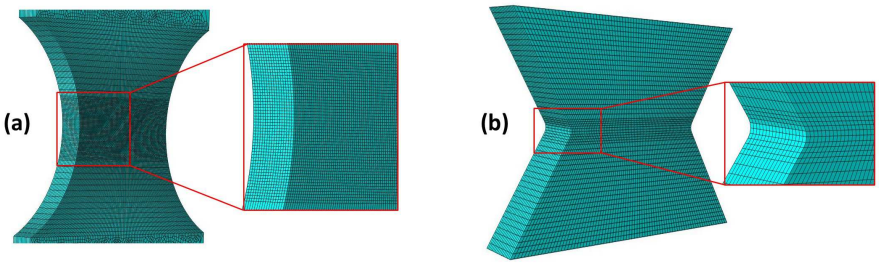

Fig. 7. FEM mesh of the notched (a) and shear (b) specimen.

Table 4 Material parameters of Ti-6Al-4V

Q	b	C	a	S_{sh}	S_{ten}	ξ_s	s	γ	β	$Y_0(MPa)$
1250.0	1.6	2000.0	20.0	16.0	25.0	1.0	2.0	4.0	2.0	0.0

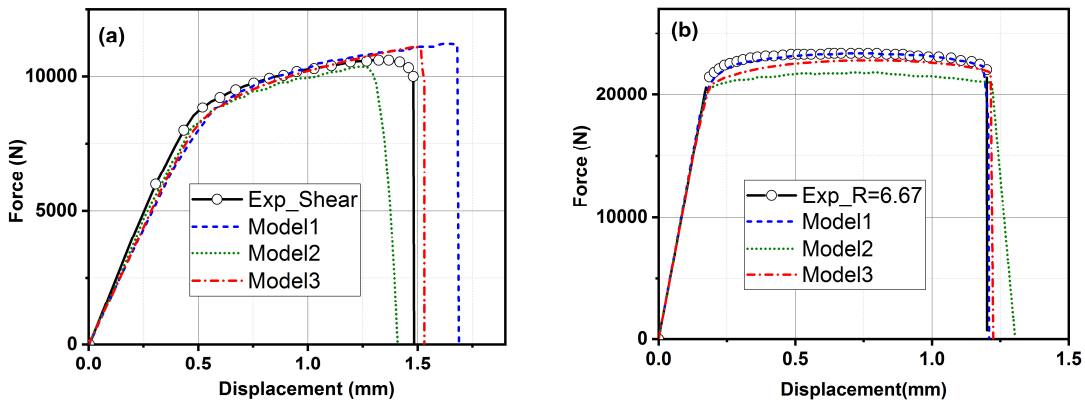

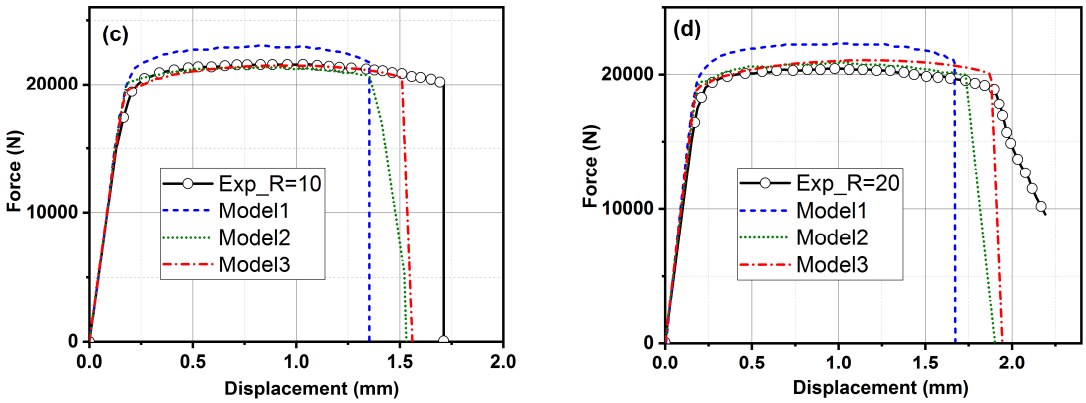

Fig. 8. Comparison of numerical and experimental responses of tensile tests at rolling direction($\theta = 0^{\circ}$): (a) shear specimen; (b) notch radius 6.67mm; (c) notch radius 10mm; (d) notch radius 20mm.

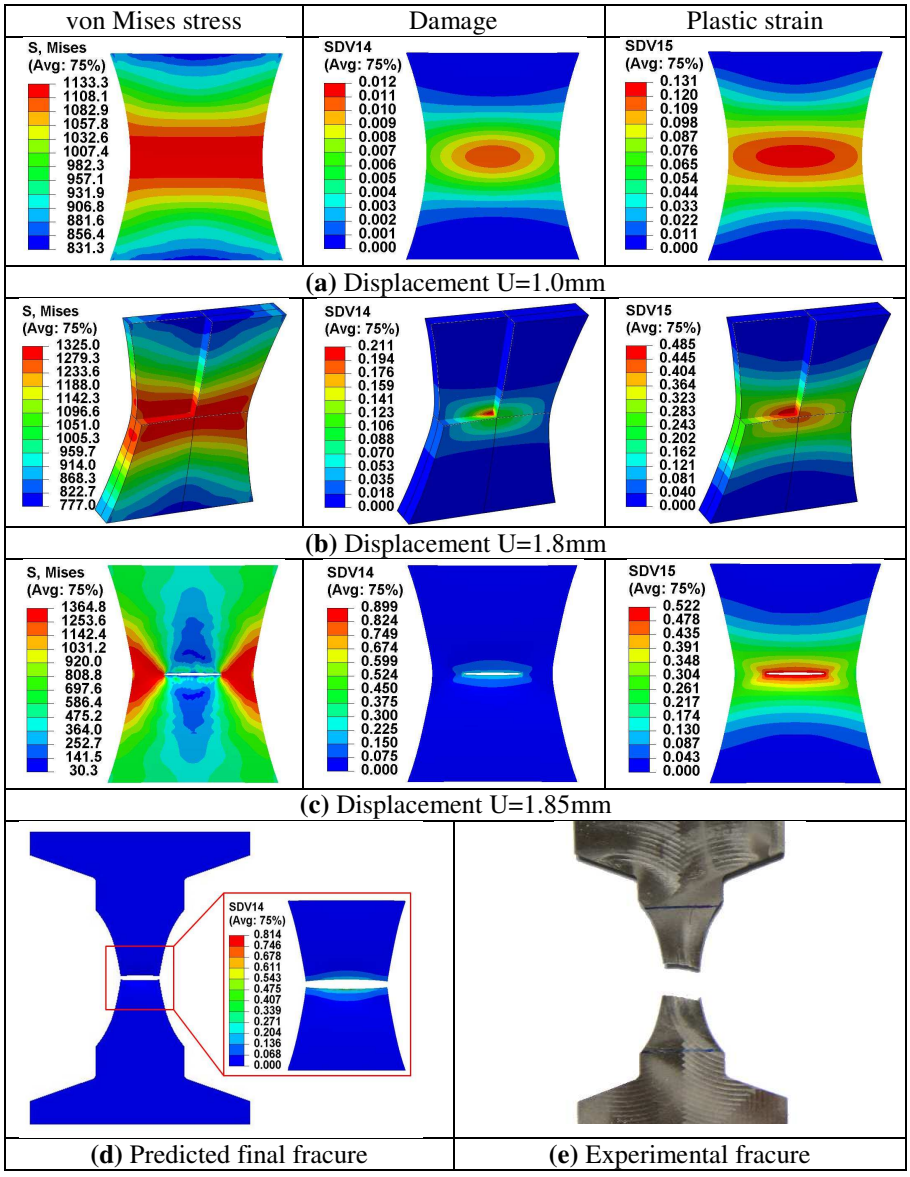

Fig. 9. Distribution of von Mises stress, damage (SDV14) and accumulated plastic strain (SDV15) for tensile specimen with notch radius 20.0 mm at different displacements.

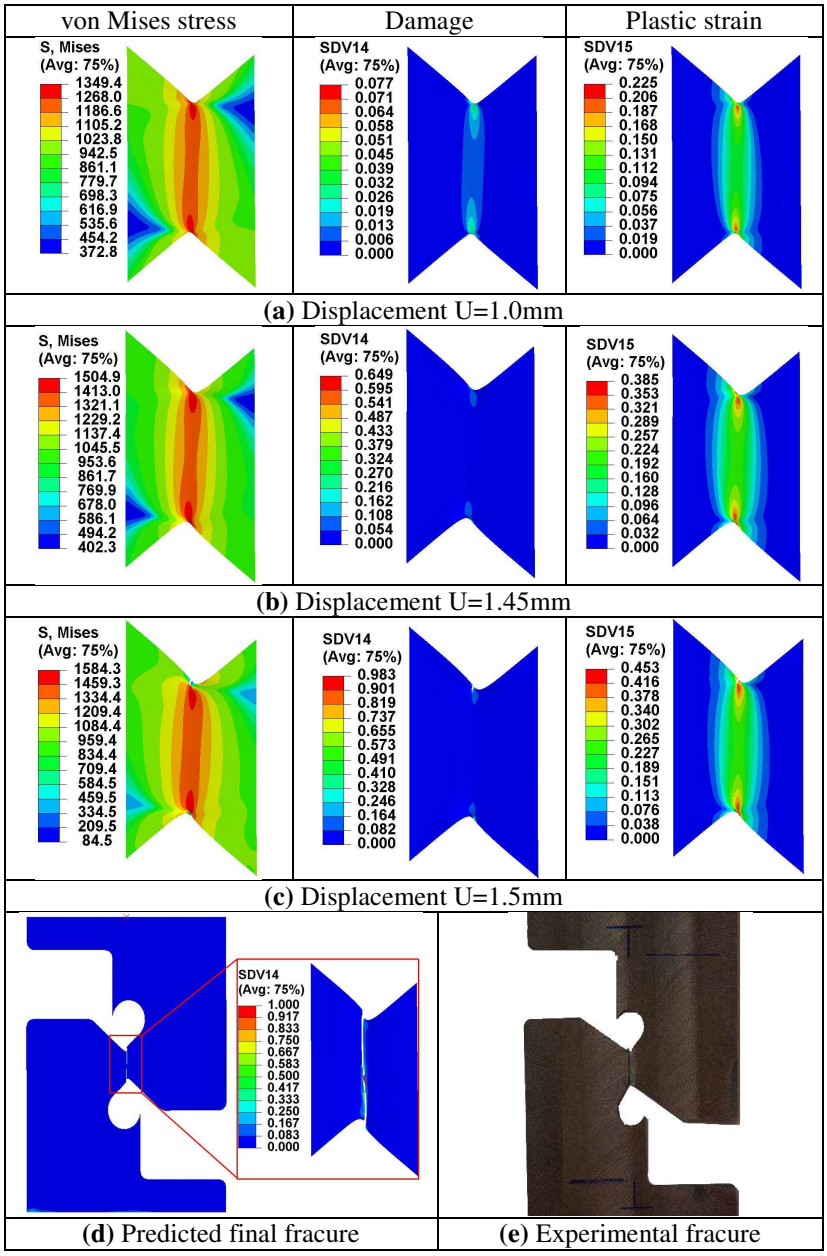

Fig. 10. Distribution of von Mises stress, damage (SDV14) and accumulated plastic strain (SDV15) for shear specimen at different displacements.

Simulations using a simple CDM damage model (Model-1) and a modified Mohr-Coulomb (MMC) damage model were performed by Allahverdizadeh et al. (2015). The simple CDM damage model has no Lode angle effect, while the MMC model (Model-2) takes the Lode angle effect into account without coupling with plastic behavior. Therefore, these results are used to compare with the new proposed enhanced Lode angle-dependent fully coupled CDM model (Model-3). As illustrated in Fig. 8, the different numerical simulation results and experimental responses of tensile tests at rolling direction ($\theta = 0^{\circ}$) are compared. All the prediction made by the three models have discrepancy with the

experimental data. For Model-1, large discrepancy was observed between the prediction results and experiments as shown in Fig. 8c and 8d, this is caused by the identification using only smooth specimen to determine all the parameters, which could not fit all other loading cases. However, the enhanced Lode angle-dependent CDM model (Model-3) shows the best fitting with experimental results compared to the other two models. Especially, the displacement at final fracture is well predicted by Model-3.

The distribution of von Mises equivalent stress, damage (SDV14) and plastic strain (SDV15) for shear and notched (R=20.0 mm) specimens of rolling direction ($\theta = 0^{\circ}$) are displayed at different displacements. As shown in Fig.9, with the increase of displacement, a strong localization of plastic flow and damage is observed at the center of the specimen where the onset of fracture takes place (damage initiation), then propagates horizontally to the edges of the notched part. As expected, a plunge of von Mises stress is observed at cracked area. The final crack path predicted by numerical simulation shows a satisfied fitting with the experimental observation. For shear specimen in Fig. 10, the localization of stress, strain and damage occurs at the two edges of the specimen. The final crack initiates at the edges of the shear specimen and evolves vertically to the center. The final crack path is well predicted by the proposed model.

4.2 Discussion of Lode angle effect on crack path

Recall the Fig. 2 which shows the effect of ($S_{ten} - S_{sh}$) on the iso-damage surfaces, at the condition $S_{sh} > S_{ten}$, the fracture locus is located outside the isotropic damage surface of $S_{ten} = S_{sh}$ (no Lode angle effect), the fracture locus likes a flower with six petals indicates that the ductile fracture tends to occur at larger values of absolute value of $\bar{\theta}_L$ when $S_{sh} > S_{ten}$. It is noteworthy that the distribution of normalized Lode angle is not homogeneous along the horizontal axis of the notched part, as shown in Fig. 11, before the cracks appear, at the two edge sides the value of $\bar{\theta}_L$ is near 1 which is much higher than that in the center not exceeding 0.5.

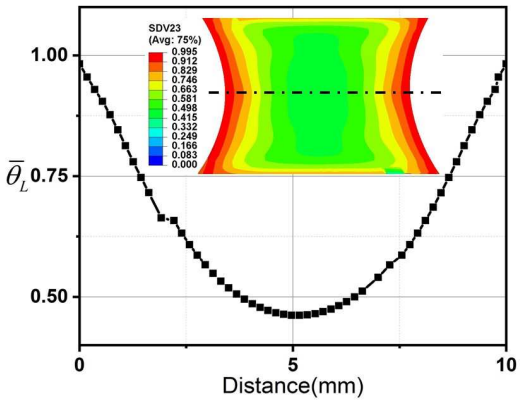

Fig. 11. Normalized Lode angle (SDV23) along the horizontal direction of the notched part.

To exploit the influence of the new proposed damage model on onset of fracture, the simulation using the specimen with notch radius 6.67mm at rolling direction is conducted under the condition ($S_{sh}=16.0, S_{ten}=8.0$, Case_1). The simulation results under the condition ($S_{sh}=16.0, S_{ten}=25.0$, Case_2) are given in Fig. 12 for comparison purpose.

The von Mises stress, damage (SDV14) and accumulated plastic strain (SDV15) distributions for the different cases are shown in Fig. 12. Before fracture occurs, the strong strain localization is found on the outer edges of the specimen for Case_1, which is quite different from the results of Case_2 (at the center of the specimen). The macroscopic crack of Case_1 starts at the two outer edges of the notched region while the onset of fracture for Case_2 is in the center area.

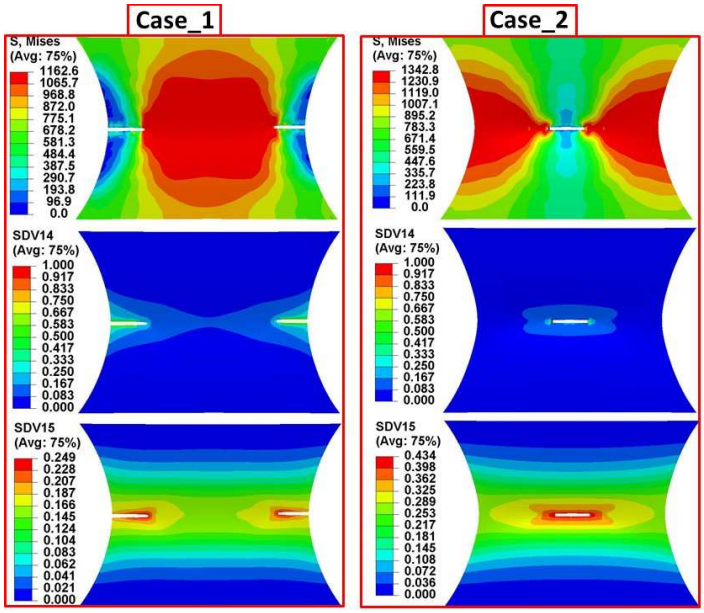

Fig. 12. Comparison of von Mises stress, damage (SDV14) and plastic strain (SDV15) for different cases of damage parameters (Case_1 with $S_{sh}=16.0, S_{ten}=8.0$; Case_2 with $S_{sh}=16.0, S_{ten}=25.0$).

For Case_1, since the normalized Lode angle ($\bar{\theta}_L \approx 1$)is high at two edges, the value of damage parameter S in Eq.(8) is smaller at two edges, which leads to a faster damage evolution at the outer edges than at the central area (where $\bar{\theta}_L \approx 0.46$), so the cracks start at the edges of the specimen for Case_1. Even though this case is not consistent with the experimental measurement for Ti-6Al-4V, it is discussed here to demonstrate the capability of the proposed model in predicting crack which starts from the outer edges and propagates to the center, as observed for aluminum alloy tests conducted by Thuillier et al. (2011).

4.3 Validation with flat specimen tensile test (FST)

In this section, the proposed model is validated through flat specimen tensile test using the calibrated material parameters for Ti-6Al-4V. This test for Ti-6Al-4V was reported in (Allahverdizadeh, 2014; Giglio et al., 2012). The mesh of the specimen is shown in Fig. 13, with mesh size 0.1 mm in the central region of the specimen.

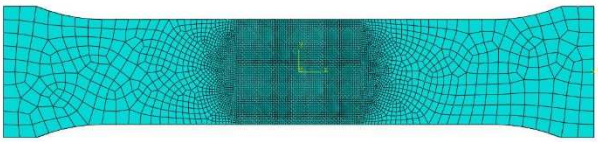

Fig. 13. Mesh of the flat specimen tensile test.

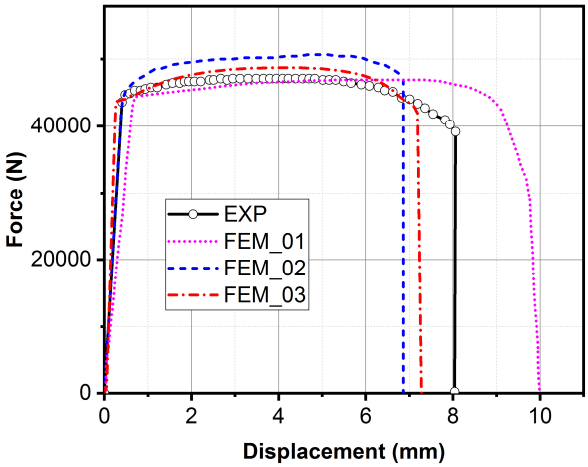

Fig. 14. Force-displacement curves for FST test from numerical simulations and experiments.

The numerical predicted force-displacement curves are compared to the experimental results, as shown in Fig. 14. The FE simulation results reported by Giglio et al. (2012) and Allahverdizadeh (2014)

are also presented with the name of 'FEM_01' and 'FEM_02'. The predicted slope of elastic deformation of 'FEM_01' shows discrepancy with experiments which could be caused by small error in their FE simulation, since fracture behavior is the focus, the small discrepancy for elastic part of the simulations is neglected. The proposed model ('FEM_03') has a better prediction of fracture compared to the result of 'FEM_01', and the hardening evolution are fitted better compared to the result of 'FEM_02'.

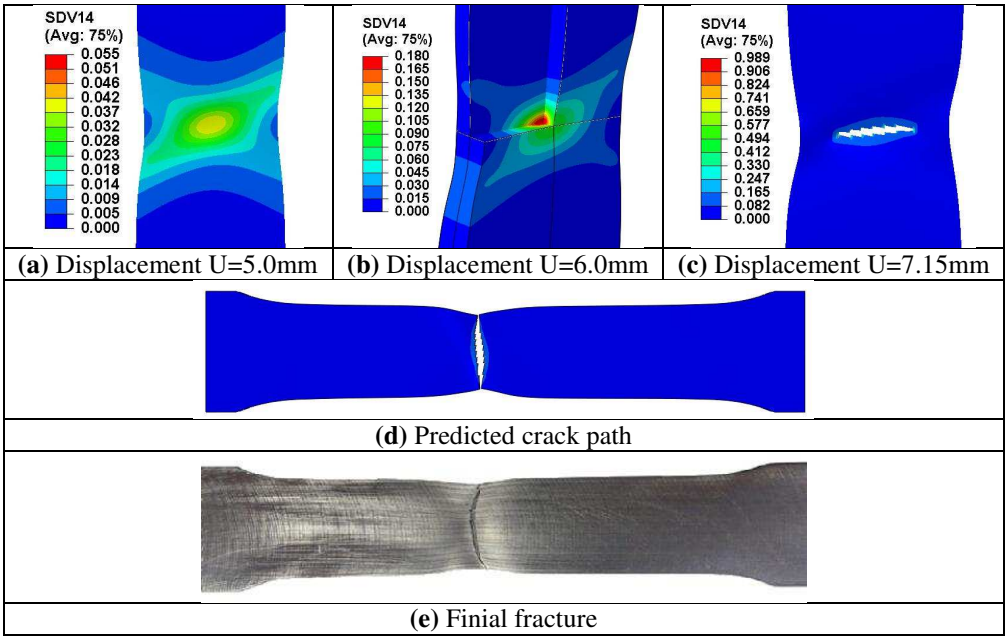

Fig. 15. The damage evolution at different displacements of FST test at rolling direction.

The damage evolution at different displacements is given in Fig. 15(a), (b) and (c), a curvature along the loading direction (diffuse necking) and a reduction of thickness (localized necking) appears with the increase of displacement. The final fracture is observed at the center of the specimen which is consistent with the experimental results in Fig. 15(d) and (e).

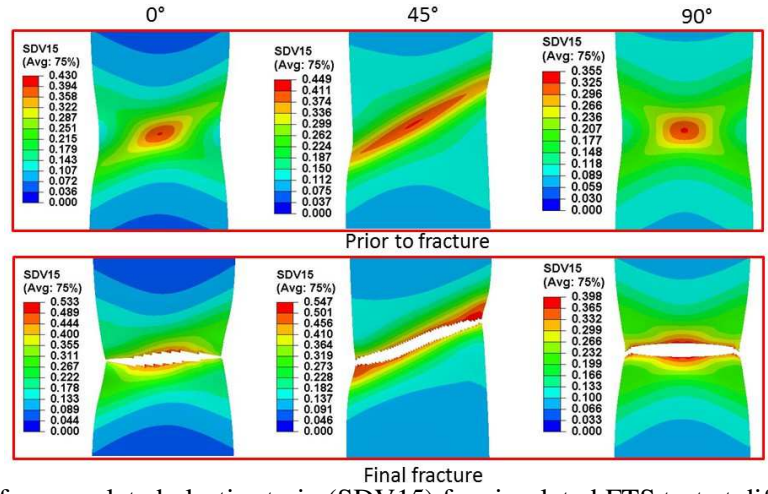

Fig. 16. Contour of accumulated plastic strain (SDV15) for simulated FTS test at different orientations.

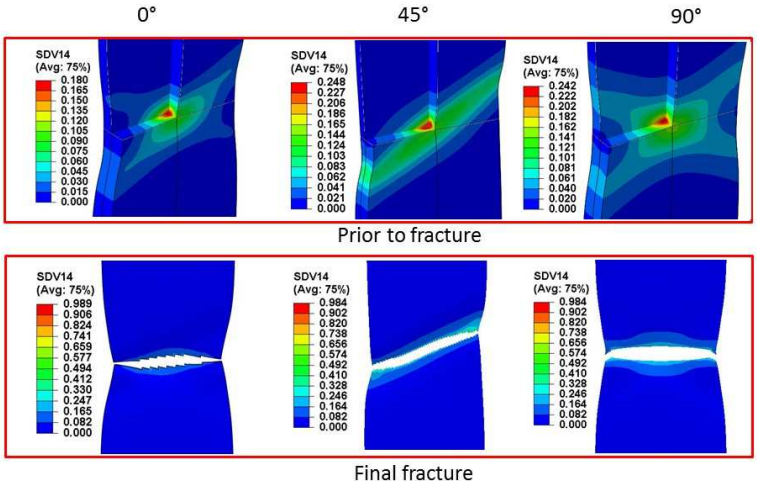

Fig. 17. Contour of damage (SDV14) for simulated FTS test at different orientations.

To highlight the influence of initial anisotropy on the final crack path, numerical simulations of FST test with various material orientations ($\theta = 0^\circ, 45^\circ$ and 90°) are conducted. The contour of accumulated plastic strain and damage are illustrated in Fig.16 and Fig.17, the plastic strain localization at 45° before fracture has huge difference with that at material orientations of 0° and 90°, the damage of three material orientations is concentrated at the center, then propagate to the edges along their strain localization paths. As a result, the final fractures of FST test at three material orientations are distinct from each other. The crack paths of 0° and 90° are relatively horizontal compared to that at 45° which has an inclined angle. Therefore, the fracture occurrence in Ti-6Al-4V sheets is affect tremendously by the initial plastic anisotropy.

4.4 Validation with three-point bending test (TPB)

A three-point bending test conducted by Giglio et al. (2012) using notched bar of Ti-6Al-4V was investigated to validate the proposed model on fracture prediction of cracked component. The numerical simulations suggest that the fracture is highly dependent on the mesh size (Allahverdizadeh et al., 2015; Giglio et al., 2012), to reduce the mesh size dependencies, we are still using the same mesh size about 0.1mm for all simulations, recall that this mesh size is used during the identification study.

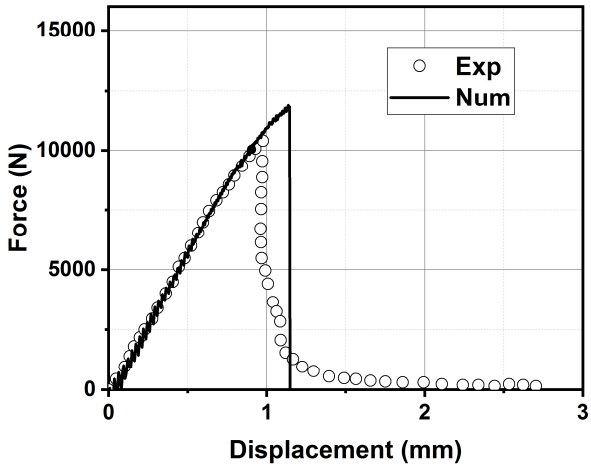

Fig. 18. Comparison between the simulation results and experiments for TPB test.

The force-displacement curves from numerical simulations and experiments for TPB test are compared in Fig. 18. The predicted result follows well the experimental curve, while the displacement at fracture is slightly overestimated. The predicted final fracture, as expected, occurs at the notch tip, which is agree with the experimental test. As shown in Fig. 19, prior to fracture, the damage is strongly localized at the notch tip, then the crack propagates vertically to a flat crack path. Base on the fact that the numerical results of TPB tests reported in the works (Allahverdizadeh et al., 2015; Giglio et al., 2012) attempt to fit the final displacement at fracture through reducing the mesh size, the numerical simulation results using the proposed damage model shows relatively satisfied accordance with the experimental results by using consistent mesh size from calibration to application.

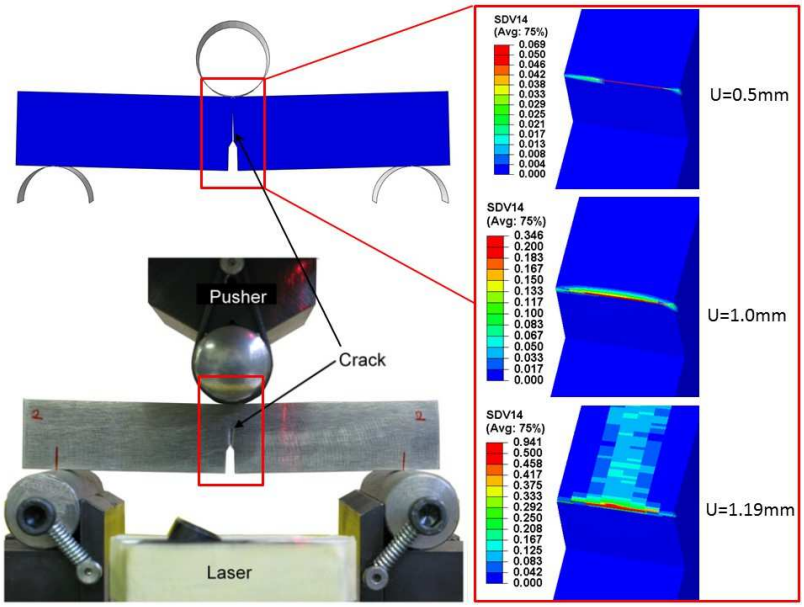

Fig. 19. Numerical predicted fracture and experimental ones for TPB test.

5. Conclusions

The anisotropic plasticity fully coupled with ductile damage behavior of Ti-6Al-4V was investigated. The established constitutive equations show their capability on describing initial anisotropy and tension-compression asymmetry. By including the Lode angle dependency to ductile damage parameter, shear fracture could be predicted using the fully coupled CDM damage model. The proposed model was calibrated with a well-designed procedure and was implemented into FE simulations for Ti-6Al-4V. Then it was applied to FST and TPB tests to validate the fracture prediction ability. The force-displacement curves from simulation results show good accordance with experimental measurements. Moreover, the fracture locations were well predicted. This model could not be limited only for Ti-6Al-4V, a more generalized version with considering microcracks closure effect is under preparation to be able to predict damage at negative stress triaxiality. Still, a simple shear test is required to determine accurately the damage parameters to increase the performance in metal forming of the developed model.

Acknowledgment

This work was supported by China Scholarship Council (201504490024), Qingdao postdoctoral applied research program, the European Funds and the Alsace-Champagne-Ardenne-Loraine Region (ESSAIMAGE D201600778).

Appendix. A

The analytic expressions of yield stresses at different orientations in tension and compression of the proposed yield function are written:

$$\sigma_\theta^T = \sigma_y / \left[K_1^{3/2} - wK_2 \right]^{1/3} \tag{A.1}$$

$$\sigma_\theta^C = \sigma_y / \left[K_1^{3/2} + wK_2 \right]^{1/3} \tag{A.2}$$

where

$$K_1 = (G+H)\cos^4\theta - 2H\cos^2\theta\sin^2\theta + (H+F)\sin^4\theta + 2N\sin^2\theta\cos^2\theta \tag{A.3}$$

$$\begin{aligned} K_2 = {} & \left(G'^2H' + G'H'^2\right)\cos^6\theta + (G'H'^2 - 2H'^2F' - H'F'^2 - F'^2G' + 4F'N'^2)\sin^4\theta\cos^2\theta + \\ & \left(H'F'^2 + H'^2F'\right)\sin^6\theta + (F'H'^2 - 2G'H'^2 - H'G'^2 - F'G'^2 + 4G'N'^2)\cos^4\theta\sin^2\theta \end{aligned} \tag{A.4}$$

σ_θ^T and σ_θ^C are uniaxial tensile and compressive yield stresses at different orientations θ from the

rolling direction in $x-y$ plane.

Lankford coefficient (R-value) in $x-y$ plane is given as follows:

$$r_\theta = \frac{\dot{\varepsilon}_w^{pl}}{\dot{\varepsilon}_t^{pl}} = \frac{\dot{\varepsilon}_{yy}^{pl}}{\dot{\varepsilon}_{zz}^{pl}} = \left(\sin^2\theta \frac{\partial f}{\partial \sigma_{xx}} - \sin 2\theta \frac{\partial f}{\partial \sigma_{xy}} + \cos^2\theta \frac{\partial f}{\partial \sigma_{yy}} \right) \Big/ \left(\frac{\partial f}{\partial \sigma_{xx}} + \frac{\partial f}{\partial \sigma_{yy}} \right) \tag{A.5}$$

The analytic expressions of Hill's criterion:

R-value: $$r_\theta = \frac{(4H'+G'+F'-2N')\cos^4\theta + (2N'-4H'-F'-G')\cos^2\theta + H'}{(G'-F')\cos^2\theta + F'} \tag{A.6}$$

Yield stress: $$\sigma_\theta = \sigma_y / [(G+F+4H-2N)\cos^4\theta + (2N-4H-2F)\cos^2\theta + H + F]^{1/2} \tag{A.7}$$

Table A.1 Anisotropy parameters for Ti-6Al-4V using Hill criterion.

F_c	G_c	H_c	N_c	F_p	G_p	H_p	N_p
0.4103	0.4677	0.5323	1.7834	0.2399	0.4677	0.5323	1.9946

Reference

Allahverdizadeh, N., 2014. Investigation of geometry transferability of Lemaitre's continuum damage mechanics model. Politecnico di Milano.

Allahverdizadeh, N., Gilioli, A., Manes, A., Giglio, M., 2015. An experimental and numerical study for the damage characterization of a Ti–6AL–4V titanium alloy. Int. J. Mech. Sci. 93, 32-47.

Badreddine, H., Saanouni, K., Dogui, A., 2010. On non-associative anisotropic finite plasticity fully coupled with isotropic ductile damage for metal forming. Int. J. Plast. 26, 1541-1575.

Bai, Y., Wierzbicki, T., 2008. A new model of metal plasticity and fracture with pressure and Lode dependence. Int. J. Plast. 24, 1071-1096.

Barlat, F., Aretz, H., Yoon, J.W., Karabin, M.E., Brem, J.C., Dick, R.E., 2005. Linear transfomation-based anisotropic yield functions. Int. J. Plast. 21, 1009-1039.

Cao, T.S., 2013. Modeling ductile damage for complex loading paths. Ecole Nationale Supérieure des Mines de Paris.

Cao, T.S., Gachet, J.M., Montmitonnet, P., Bouchard, P.O., 2014. A Lode-dependent enhanced Lemaitre model for ductile fracture prediction at low stress triaxiality. Eng. Fract. Mech. 124-125, 80-96.

Cazacu, O., Barlat, F., 2004. A criterion for description of anisotropy and yield differential effects in pressure-insensitive metals. Int. J. Plast. 20, 2027-2045.

Cazacu, O., Plunkett, B., Barlat, F., 2006. Orthotropic yield criterion for hexagonal closed packed metals. Int. J. Plast. 22, 1171-1194.

Ghorbel, O., Koubaa, S., Mars, J., Wali, M., Dammak, F., 2019. Non associated-anisotropic plasticity model fully coupled with isotropic ductile damage for sheet metal forming applications. Int. J. Solids Struct. 166, 96-111.

Giglio, M., Manes, A., Viganò, F., 2012. Ductile fracture locus of Ti–6Al–4V titanium alloy. Int. J. Mech. Sci. 54, 121-135.

Gilles, G., Hammami, W., Libertiaux, V., Cazacu, O., Yoon, J.H., Kuwabara, T., Habraken, A.M., Duchêne, L., 2011. Experimental characterization and elasto-plastic modeling of the quasi-static mechanical response of TA-6V at room temperature. Int. J. Solids Struct. 48, 1277-1289.

Gurson, A.L., 1977. Continuum theory of ductile rupture by void nucleation and growth: Part I—Yield criteria and flow rules for porous ductile media. J. Eng. Mat. Tech. 99, 2-15.

Hill, R., 1948. A theory of the yielding and plastic flow of anisotropic metals. Proc. R. Soc. Lond. Ser. A 193, 281-297.

Johnson, G.R., Cook, W.H., 1985. Fracture characteristics of three metals subjected to various strains, strain rates, temperatures and pressures. Eng. Fract. Mech. 21, 31-48.

Khan, A.S., Kazmi, R., Farrokh, B., 2007. Multiaxial and non-proportional loading responses, anisotropy and modeling of Ti–6Al–4V titanium alloy over wide ranges of strain rates and temperatures. Int. J. Plast. 23, 931-950.

Kuwabara, T., Saito, R., Hirano, T., Oohashi, N., 2009. Difference in tensile and compressive flow stresses in austenitic stainless steel alloys and its effect on springback behavior. Int. J. Mater. Form. 2, 499-502.

Lemaitre, J., 1985. A continuous damage mechanics model for ductile fracture. Trans ASME. J. Eng. Mater. Tech. 107, 83-89.

Lemaitre, J., Chaboche, J.-L., 1994. Mechanics of solid materials. Cambridge University Press.

Lou, Y., Huh, H., 2013. Prediction of ductile fracture for advanced high strength steel with a new criterion: Experiments and simulation. Journal of Materials Processing Tech. 213, 1284-1302.

Malcher, L., Mamiya, E.N., 2014. An improved damage evolution law based on continuum damage mechanics and its dependence on both stress triaxiality and the third invariant. Int. J. Plast. 56, 232-261.

Plunkett, B., Cazacu, O., Barlat, F., 2008. Orthotropic yield criteria for description of the anisotropy in tension and compression of sheet metals. Int. J. Plast. 24, 847-866.

Saanouni, K., 2006. Virtual metal forming including the ductile damage occurrence : Actual state of the art and main perspectives. J. Mater. Process. Technol. 177, 19-25.

Saanouni, K., 2012. Damage mechanics in metal forming: Advanced modeling and numerical simulation. John Wiley & Sons.

Saanouni, K., Hamed, M., 2013. Micromorphic approach for finite gradient-elastoplasticity fully coupled with ductile damage: Formulation and computational aspects. Int. J. Solids Struct. 50, 2289-2309.

Soyarslan, C., Richter, H., Bargmann, S., 2016. Variants of Lemaitre's damage model and their use in formability prediction of metallic materials. Mechanics of Materials 92, 58-79.

Steglich, D., Brocks, W., Bohlen, J., Barlat, F., 2011. Modelling direction-dependent hardening in magnesium sheet forming simulations. Int. J. Mater. Form. 4, 243-253.

Taherizadeh, A., Green, D.E., Yoon, J.W., 2015. A non-associated plasticity model with anisotropic and nonlinear kinematic hardening for simulation of sheet metal forming. Int. J. Solids Struct. 69-70, 370-382.

Thuillier, S., Le Maoût, N., Manach, P.Y., 2011. Influence of ductile damage on the bending behaviour of aluminium alloy thin sheets. Mater Design 32, 2049-2057.

Traphöner, H., Clausmeyer, T., Tekkaya, A.E., 2018. Material characterization for plane and curved sheets using the in-plane torsion test – An overview. J. Mater. Process. Technol. 257, 278-287.

Tvergaard, V., Needleman, A., 1984. Analysis of the cup-cone fracture in a round tensile bar. Acta metallurgica 32, 157-169.

Xue, L., Wierzbicki, T., 2008. Ductile fracture initiation and propagation modeling using damage plasticity

theory. Eng. Fract. Mech. 75, 3276-3293.

Yin, Q., Soyarslan, C., Isik, K., Tekkaya, A.E., 2015. A grooved in-plane torsion test for the investigation of shear fracture in sheet materials. Int. J. Solids Struct. 66, 121-132.

Yoon, J.W., Lou, Y., Yoon, J., Glazoff, M.V., 2014. Asymmetric yield function based on the stress invariants for pressure sensitive metals. Int. J. Plast. 56, 184-202.

Yue, Z., Cao, K., Badreddine, H., Saanouni, K., Gao, J., 2019. Failure prediction on steel sheet under different loading paths based on fully coupled ductile damage model. Int. J. Mech. Sci. 153-154, 1-9.

Yue, Z., Soyarslan, C., Badreddine, H., Saanouni, K., Tekkaya, A., 2015. Identification of fully coupled anisotropic plasticity and damage constitutive equations using a hybrid experimental–numerical methodology with various triaxialities. Int. J. Damage Mech. 24, 683-710.

Zhang, K., Badreddine, H., Saanouni, K., 2018. Thermomechanical modeling of distortional hardening fully coupled with ductile damage under non-proportional loading paths. Int. J. Solids Struct. 144, 123-136.

Zhang, K., Badreddine, H., Saanouni, K., 2019. Thermodynamically-consistent constitutive modeling of hardening asymmetry including isotropic ductile damage for Mg alloys. Eur. J. Mech. A Solids 73, 169-180.

Zhuang, X., Meng, Y., Zhao, Z., 2017. Evaluation of prediction error resulting from using average state variables in the calibration of ductile fracture criterion. Int. J. Damage Mech. 27, 1231-1251.